A 3-D model of the crust and uppermost mantle beneath the Central and Western US by joint inversion of receiver functions and surface wave dispersion

Weisen Shen,[1] Michael H. Ritzwoller,[1] and Vera Schulte-Pelkum[2]

[1] Rayleigh wave phase velocity maps from ambient noise and earthquake data are inverted jointly with receiver functions observed at 828 stations from the USArray Transportable Array west of 100°W longitude for data recorded in the years 2005 through 2010 to produce a 3-D model of shear wave speeds beneath the central and Western US to a depth of 150 km. Eikonal tomography is applied to ambient noise data to produce about 300,000 Rayleigh wave phase speed curves, and Helmholtz tomography is applied to data following 1550 (Ms > 5.0) earthquakes so that Rayleigh wave dispersion maps are constructed from 8 to 80 s period with associated uncertainties across the region. Harmonic stripping generates back-azimuth independent receiver functions with uncertainty estimates for each of the stations. A nonlinear Bayesian Monte Carlo method is used to estimate a distribution of shear wave speed (Vs) models beneath each station by jointly interpreting surface wave dispersion and receiver functions and their uncertainties. The assimilation of receiver functions improves the vertical resolution of the model by reducing the range of estimated Moho depths, improving the determination of the shear velocity jump across Moho, and improving the resolution of the depth of anomalies in the uppermost mantle. A great variety of geological and tectonic features are revealed in the 3-D model that form the basis for future detailed local to regional scale analysis and interpretation.

1. Introduction

[2] Continental-scale arrays of seismometers with interstation spacings between 50 and 100 km such as the EarthScope USArray Transportable Array (TA), the Chinese Earthquake Array, the Virtual European Broadband Seismic Network, or for that matter PASSCAL or USArray Flexible Array experiments that in some cases comprise more than 100 instruments, providing ideal data for surface wave tomography. The combination of ambient noise measurements, typically between about 8 and 40 s period (e.g., in the US: *Shapiro et al.* [2005]; *Moschetti et al.* [2007]; *Lin et al.* [2008]; *Bensen et al.* [2008]), and earthquake-derived measurements, from about 25 to 100 s period (e.g., in the US: *Pollitz* [2008]; *Lin et al.* [2009]; *Lin and Ritzwoller* [2011a]), produces broadband dispersion maps that constrain earth structure homogeneously through the crust to a depth of about 150 km in the uppermost mantle. Such broadband measurements from ambient noise and/or earthquake data observed with USArray have been used by *Yang et al.* [2008], *Pollitz and Snoke* [2010], *Moschetti et al.* [2010a, 2010b], *Lin et al.* [2010], *Obrebski et al.* [2011], and others to produce 3-D shear velocity models of the crust and uppermost mantle in the Western US.

[3] The use of surface wave dispersion data alone to produce models of the crust and uppermost mantle, however, presents significant non-uniqueness problems (e.g., *Shapiro et al.* [2002] and many others) because surface waves do not constrain the strength or location of jumps in shear velocity. Receiver functions, in contrast, provide the spatially discrete local response of seismic waves to discontinuities beneath receiver locations [*Langston*, 1979]. As a consequence, combining surface wave data with receiver function data has been a natural direction for research and was introduced more than a decade ago [e.g., *Last et al.*, 1997; *Julia et al.*, 2000; *Ozalaybey et al.*, 1997], with numerous realizations of the idea subsequently having been developed. In particular, joint inversions of receiver functions and surface wave dispersion within the context of nonlinear, model-space sampling schemes have been developed in recent years [e.g., *Chang et al.*, 2004; *Lawrence and Wiens*, 2004; *Liu et al.*, 2010; *Tokam et al.*, 2010; *Bodin et al.*, 2012; *Shen et al.*, 2013].

[1]Department of Physics, University of Colorado at Boulder, Boulder, Colorado, USA.
[2]Cooperative Institute for Research in Environmental Sciences and Department of Geological Sciences, University of Colorado at Boulder, Boulder, Colorado, USA.
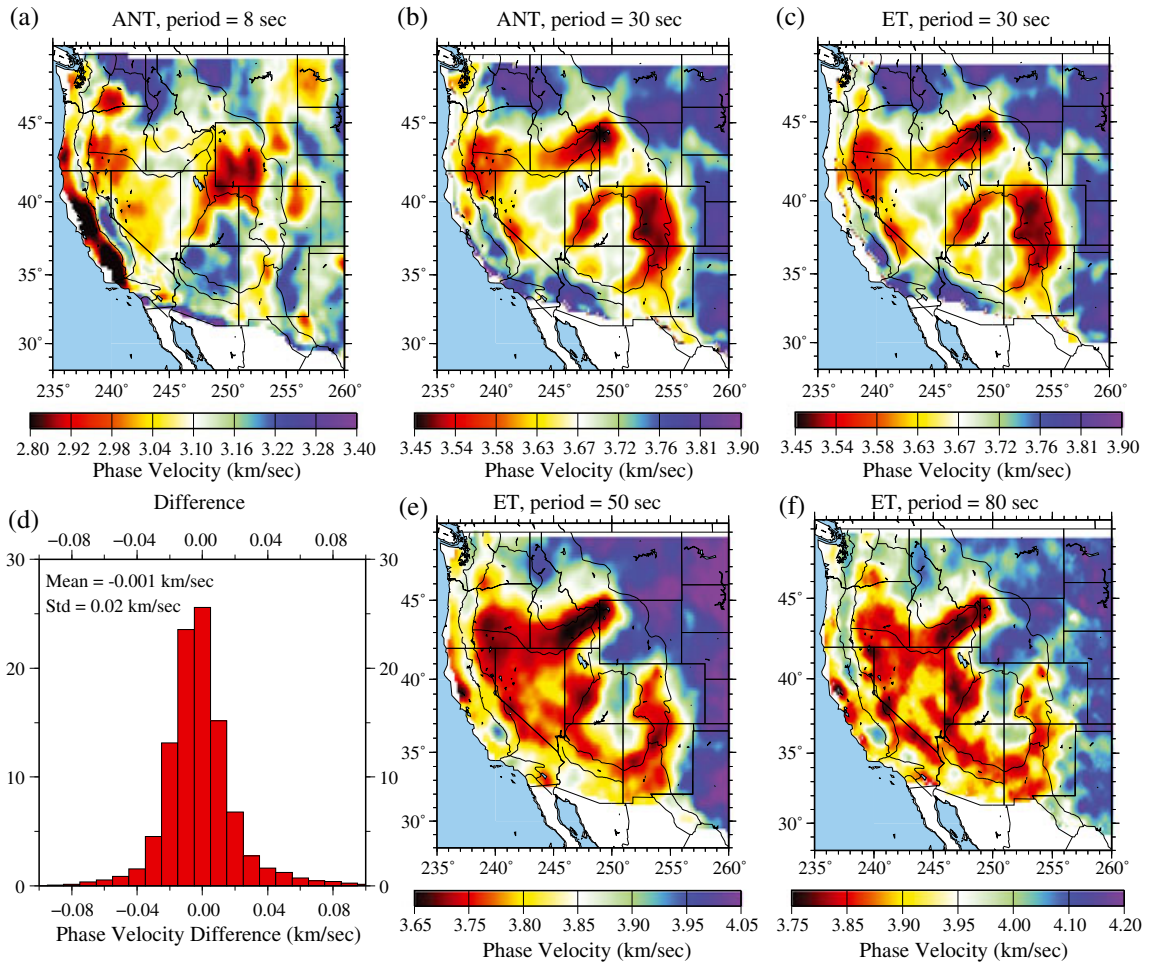
Corresponding author: W. Shen, Department of Physics, University of Colorado at Boulder, Boulder, CO 80309-0390, USA. (weisen.shen@colorado.edu)

[4] *Shen et al.* [2013] presents a nonlinear Bayesian Monte Carlo method to estimate a Vs model with uncertainties beneath stations by jointly interpreting surface wave dispersion and receiver functions and associated uncertainties. This method is designed for automated application to large arrays of broadband seismometers. Here, we apply this method to the joint inversion of surface wave dispersion maps and receiver functions with observations taken from 828 stations of the USArray TA as well as USArray reference network stations. The region of study extends eastward from the Pacific coast to 100°W longitude and covers the entire Western US including parts of the Great Plains. This region extends about 1000 km eastward from earlier studies [*Yang et al.*, 2008; *Moschetti et al.*, 2010a, 2010b] and includes data acquired through the year 2010, adding more than 2 years of TA data compared to these earlier studies. Significantly, as discussed here, the introduction of receiver functions into the inversion with surface wave dispersion data from ambient noise and earthquake data significantly improves the vertical resolution of the model, revealing higher fidelity images of the crust and uppermost mantle across nearly half of the US.

2. Generation of the 3-D Model by Joint Inversion

2.1. Surface Wave Data

[5] Rayleigh wave phase velocity measurements from 8 to 40 s period were acquired from ambient noise using USArray TA stations deployed from the beginning of 2005 until the end of 2010. The data processing procedures described by *Bensen et al.* [2007] and *Lin et al.* [2008] were used to produce nearly 300,000 dispersion curves between the 828 TA stations west of 100°W longitude and USArray backbone (or reference network) stations. Eikonal tomography [*Lin et al.*, 2009] produced Rayleigh wave phase velocity maps for ambient noise from 8 to 40 s period (e.g., Figures 1a and 1b). Eikonal tomography is a geometrical ray theoretic technique that models off-great-circle propagation but not finite frequency effects (e.g., wavefront healing, back-scattering, etc.). Rayleigh wave phase velocity measurements from 25 to 80 s period were obtained following earthquakes using the Helmholtz tomography method [*Lin and Ritzwoller*, 2011a, 2011b], also applied to TA data from 2005 through 2010. Example dispersion maps
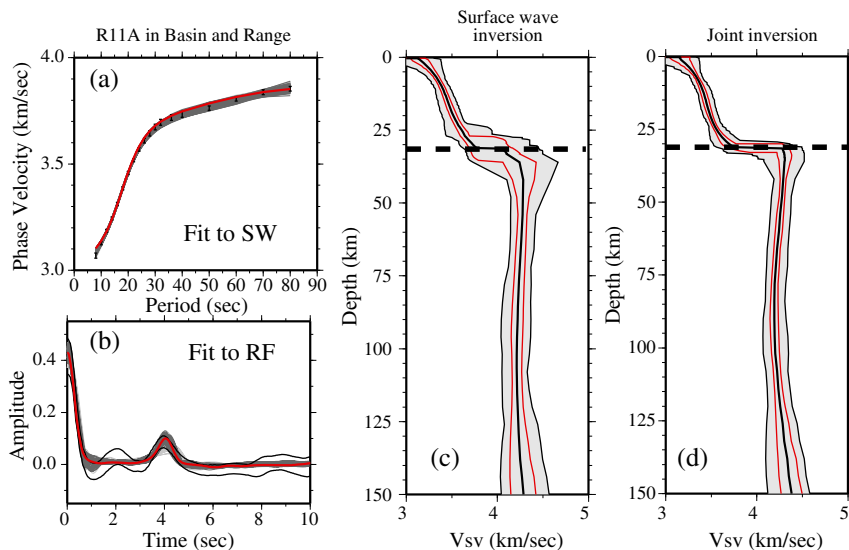

Figure 1. Example Rayleigh wave phase speed maps determined from (a, b) ambient noise data using eikonal tomography (ANT) and (c, e, and f) earthquake data using Helmholtz tomography (ET) at the periods indicated. (d) Histogram of the differences in phase speeds at 30 s period using ambient noise and earthquake data: mean difference is −1 m/s, and the standard deviation of the difference is 20 m/s. Geological provinces are delineated by black lines in the maps.

are shown in Figures 1c, 1e, and 1f. A total of 1550 earthquakes were used with magnitude $M_s > 5.0$, of which on average about 270 earthquakes supplied measurements at each location. Helmholtz tomography is a finite frequency method that accounts for wavefield complexities that affect longer period surface waves, but *Lin and Ritzwoller* [2011a, 2011b] and *Ritzwoller et al.* [2011] argue that below about 40 s period such corrections are not required.

[6] Ambient noise and earthquake phase velocity maps overlap between periods of 25 and 40 s. In this period band of overlap, the two measurements are averaged at each location based on their uncertainties. Uncertainties in Rayleigh wave dispersion maps derived from ambient noise average about 15 m/s between periods of 10 and 25 s, and uncertainties of earthquake-derived maps also average about 15 m/s but between periods of 30 and 60 s. At periods shorter and longer than these, uncertainties in each type of measurement grow. Therefore, the uncertainty of the combined measurements is approximately flat, on average, at 15 m/s from 10 to 60 s period but grows at shorter and longer periods. An example of a dispersion curve with error bars at a point in the Basin and Range province is shown in Figure 2a. In the period band of overlap, the ambient noise and earthquake-derived maps agree approximately as well as expected given uncertainties in the maps, as Figures 1b, 1c, and 1d illustrate at 30 s period. The standard deviation of the difference between the maps is 20 m/s (Figure 1d), consistent with the estimated uncertainty (~15 m /s) at 30 s period.

2.2. Receiver Functions

[7] Single station receiver functions are constructed at each of the 828 TA stations west of 100°W longitude using the method detailed as described by *Shen et al.* [2013] and briefly summarized here. Earthquakes are used if they occur between 30° and 90° from the station with mb > 5.0 during the lifetime of the station deployment. A time domain deconvolution method [*Ligorria and Ammon*, 1999] is applied to each seismogram windowed between 20 s before and 30 s after the *P*-wave arrival to calculate the radial component receiver functions with a low-pass Gaussian filter width of 2.5 s (pulse width ~1 s). Corrections are made both to the time and amplitude of each receiver function, normalizing to a reference slowness of 0.06 s/km [*Jones and Phinney*, 1998]. The receiver function waveform is discarded after 10 s because the slowness correction is appropriate for direct *P*-to-*S* conversions but not for reverberations, and later arriving Moho reverberations are thus stacked down. An azimuthally independent receiver function, $R_0(t)$, for each station is computed by fitting a truncated Fourier Series at each time over azimuth and stripping the azimuthally variable terms using a method referred to as "harmonic stripping" [*Shen et al.*, 2013], which exploits the azimuthal harmonic behavior in receiver functions [e.g., *Girardin and Farra*, 1998; *Bianchi et al.*, 2010]. After removing the azimuthally variable terms at each time, the RMS residual over azimuth is taken as the 1σ uncertainty at that time. *Shen et al.* [2013] describes procedures to assess and guarantee the quality of the receiver functions. On average, about 130 earthquakes satisfy the

Figure 2. Example outcome of the joint inversion at USArray TA station R11A in the Basin and Range province in Currant, Nevada (38.35, −115.59). (a) Observed Rayleigh wave phase speed curve presented as 1σ error bars. Predictions from the ensemble of accepted models in Figure 2d are shown (gray lines), as is the prediction from the best fitting model (red line). (b) The azimuthally independent receiver function $R_0(t)$ is shown with the black lines defining the estimated 1σ uncertainty. Predictions from the members of the ensemble in Figure 2b are shown with gray lines, and the red line is the best fitting member of the ensemble. (c) Ensemble of accepted model using surface wave data alone. The full width of the ensemble is presented as black lines enclosing a gray-shaded region, the 1σ ensemble is shown with red lines, and the average model is the black curve near the middle of the ensemble. Moho is identified as a dashed line at ~32 km. (d) Ensemble of accepted models from the joint inversion.

quality control provisions for each station across the region of study. An example of an azimuthally independent receiver function for a station in the Basin and Range province is shown in Figure 2b as a pair of locally parallel black lines, which delineate the uncertainty at each time.

2.3. Model Parameterization

[8] As a matter of practice, we seek models that have no more vertical structure than required to fit the data within a tolerance specified by the data uncertainties. At all points, we attempt to fit the data with the same parameterization. There is one sedimentary layer with a linear velocity gradient with depth. Three parameters are used to describe this layer: layer thickness and vertically polarized shear wave speed (Vsv) at the top and bottom of the layer. There is one crystalline crustal layer described by five parameters: layer thickness (km) and four B-splines for Vsv. Finally, there is one uppermost mantle layer to a depth of 200 km described by five B-splines for Vsv. The smoothness of the model is imposed by the parameterization so that ad hoc damping is not needed during the inversion. In some places, the model, which contains no discontinuities between the base of the sediments and the Moho and none in the mantle, may be too simple to fit the receiver function well or the dispersion data and receiver function jointly. We present examples of these types of cases below, and they provide the justification for an adaptive parameterization, which is used, for example, by *Bodin et al.* [2012].

[9] Because only Rayleigh waves are used, there is predominant sensitivity to Vsv rather than horizontally polarized shear wave speed (Vsh), and we assume an isotropic Vsv model where Vs = Vsh = Vsv. We set the Vp/Vs ratio to 2.0 in the sedimentary layer and 1.75 in the crystalline crust and mantle. Reasonable variations around these values [e.g., *Brocher*, 2008] will produce little change in the isotropic shear wave speeds in the crust but, as discussed by *Shen et al.* [2013], may change crustal thickness by up to 2 km in unusual circumstances. This value, however, lies within the estimated uncertainties for crustal thickness. For density, we use a scaling relation in the crust that has been influenced by the studies of *Christensen and Mooney* [1995] and *Brocher* [2005] and by *Karato* [1993] in the mantle where sensitivity to density structure is much weaker than in the crust. We also apply a physical dispersion correction [*Kanamori and Anderson*, 1977] using the Q model from PREM [*Dziewonski and Anderson*, 1981]. The biggest deviations of Q from PREM probably occur in the uppermost mantle in regions of thin lithosphere, such as in the Basin and Range province. In such regions, low Q asthenosphere may extend nearly all the way upward to the crust. Replacing lithospheric $Q = 400$ from PREM between Moho and 80 km depth with $Q = 100$ would increase Vs estimated at 60 km depth in the Basin and Range province by less than 1%. This value also lies within stated 1σ uncertainties, but the inclusion of a more realistic Q model is a fruitful direction for future research. The model is reduced to 1 s period.

2.4. Prior and Posterior Distributions of Models

[10] Prior models for Monte Carlo sampling are defined relative to a reference model [*Shapiro and Ritzwoller*, 2002] subject to allowed perturbations (presented in Table 1 of *Shen et al.* [2013]) and model constraints. Constraints are that models are continuous between discontinuities at the base of the sediments and Moho and continuous in the mantle, and velocity increases linearly with depth in the sedimentary layer and monotonically with depth in the crystalline crust. The velocity contrasts across the sedimentary basement and across the Moho discontinuity are constrained to be positive and Vs < 4.9 km/s throughout the model. Examples of marginal prior distributions for several model variables are presented in Figure 3 as white histograms.
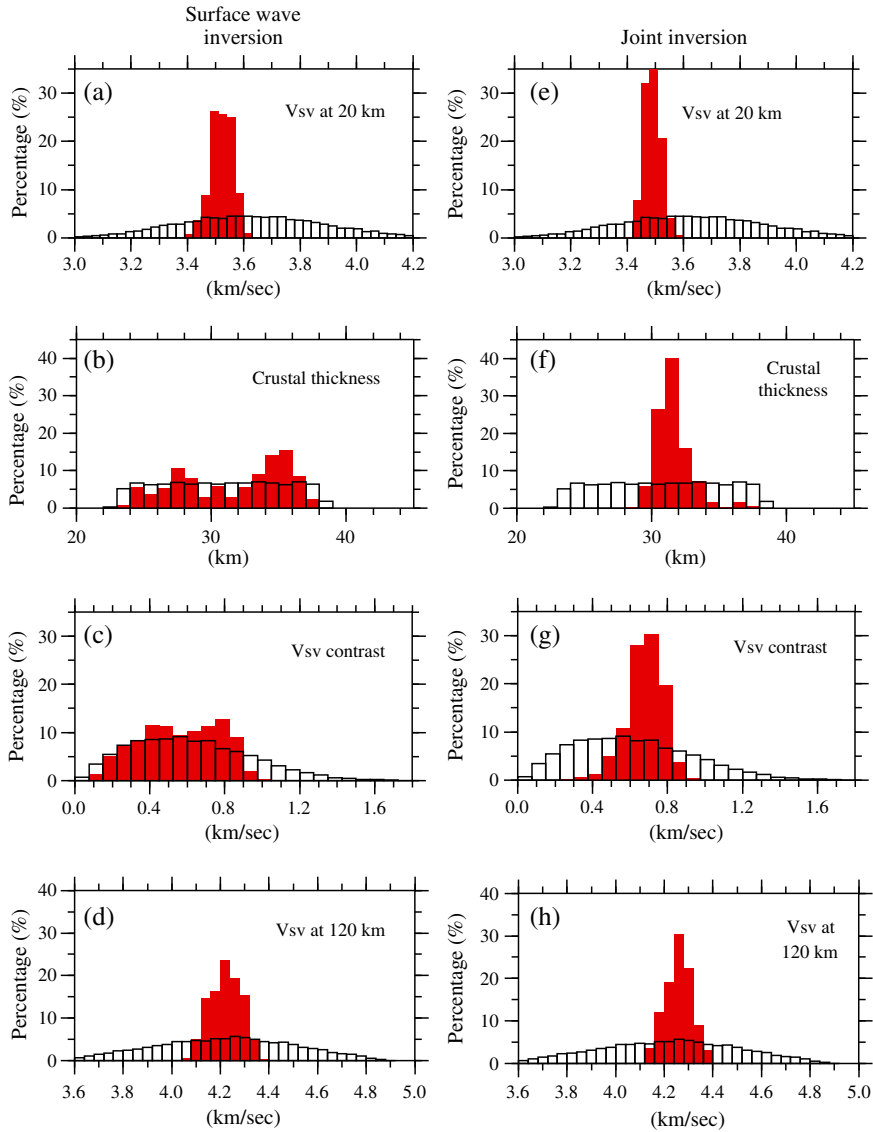
[11] The Bayesian Monte Carlo joint inversion method described by *Shen et al.* [2013] constructs a prior distribution of models at each location defined by allowed perturbations relative to the reference model as well as model constraints. The principal output is the posterior distribution of models that satisfy the receiver function and surface wave dispersion data within tolerances that depend on data uncertainties. The statistical properties of the posterior distribution quantify model errors. Examples of prior and posterior distributions for the inversion based on surface wave data alone are shown in Figures 3a–3c, which illustrate that surface wave data alone do not constrain well crustal thickness or the jump in Vs across Moho but do determine Vs between discontinuities. In contrast, when receiver functions (e.g., Figure 2b) and surface wave dispersion data (e.g., Figure 2a) are applied jointly, crustal thickness and the Vs jump across Moho are much more tightly constrained (Figures 3d–3f).

[12] The details depend on the nature of the receiver function, but on average the vertical discontinuity structure of the crust is clarified, and the vertical resolution of the model is improved by introducing receiver functions into the inversion with surface wave dispersion data. Figures 2c and 2d present examples of model ensembles for a point in the Basin and Range province based on surface wave data alone compared with surface wave and receiver function data used jointly. Consistent with the observations of the marginal distributions shown in Figure 3, the introduction of receiver functions sharpens the image around the Moho, which reduces the trade-off between model variables in the lower crust and uppermost mantle, clarifying the thickness of the crust, the jump in Vs across the Moho, and reducing the spread of model velocities in the mantle.

[13] Examples at other locations of data and resulting ensembles of models are presented by *Shen et al.* [2013] (in the Denver Basin, the Colorado Plateau, the Great Plains) and in Figures 4 and 5 here for complementary geological settings. The receiver functions in Figures 4a–4e are typical and well-behaved in that the azimuthal variability is simple enough that the uncertainties are small and the azimuthally independent receiver function is well defined. At these locations, the surface waves and receiver functions can be fit well simultaneously, and the introduction of receiver functions reduces the extent of the ensemble of accepted models, which are presented in Figures 5a–5e.

2.5. Places Where Receiver Function Uncertainties Are Large

[14] In some locations, however, the receiver function is dominated by azimuthal variability so that uncertainties are very large. An example is seen in Figure 4f for a station in the Basin and Range province. For this station, lateral heterogeneity between the local basin and the adjacent mountain range is large enough to vitiate the azimuthally

Surface wave
inversion

Joint inversion

Figure 3. (a–d) Prior and posterior (surface waves only) marginal distributions of three model variables are presented with white and red histograms, respectively, for Vsv at 20 km depth, crustal thickness, the Vsv contrast across Moho, and Vsv at 120 km depth. (e–h) Same as Figures 3a–3d but the red histogram is for the posterior marginal distribution resulting from the joint inversion of receiver functions and surface wave phase velocities.
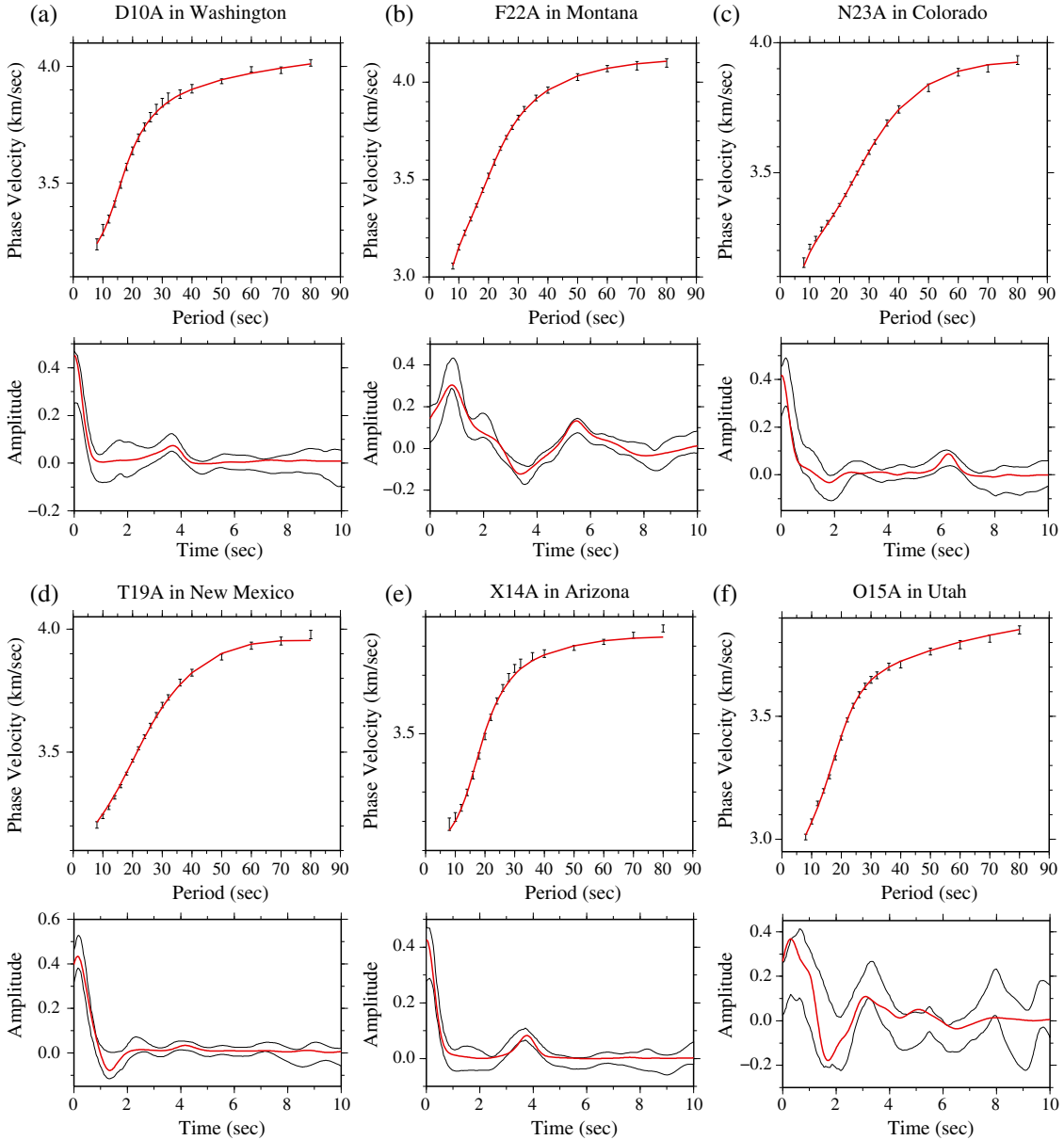
independent receiver function, and the joint inversion reverts principally to fitting the surface wave data alone. At this point, the time-averaged uncertainty in the receiver function is about 0.11, which is the average half width of the corridor of the receiver function. As a consequence, the ensemble of models is somewhat broader in Figure 5f than at locations with a more accurate receiver function (e.g., Figures 5e).

[15] Such problems with receiver functions are relatively rare and mostly appear at discrete points rather than covering large regions. Figure 6a identifies the stations where the time-averaged uncertainty is larger than 0.07, which occurs for about 10% of the stations on the map. Stations where receiver function uncertainty is large because of sharp lateral variations appear in the Pacific Northwest, in parts of the Basin and Range province, and near the edges of the Rocky Mountain province. Large receiver function uncertainties

also appear in the northern Great Plains because of the reduction in the number of azimuthally dependent receiver functions caused by the greater distance from southwestern Pacific earthquakes. Even with relatively large uncertainties, however, the receiver functions provide important information in the inversion but weaker constraints than at places where uncertainties are smaller.

2.6. Fit to the Data

[16] Surface wave data are fit acceptably in the joint inversion except near the far western periphery of the region where dispersion maps from ambient noise and earthquake tomography are most different in the period band of overlap. We believe this is caused mostly by degradation of the ambient noise maps due to azimuthal compression near the coast. In total, 817 out of the 829 stations have a surface
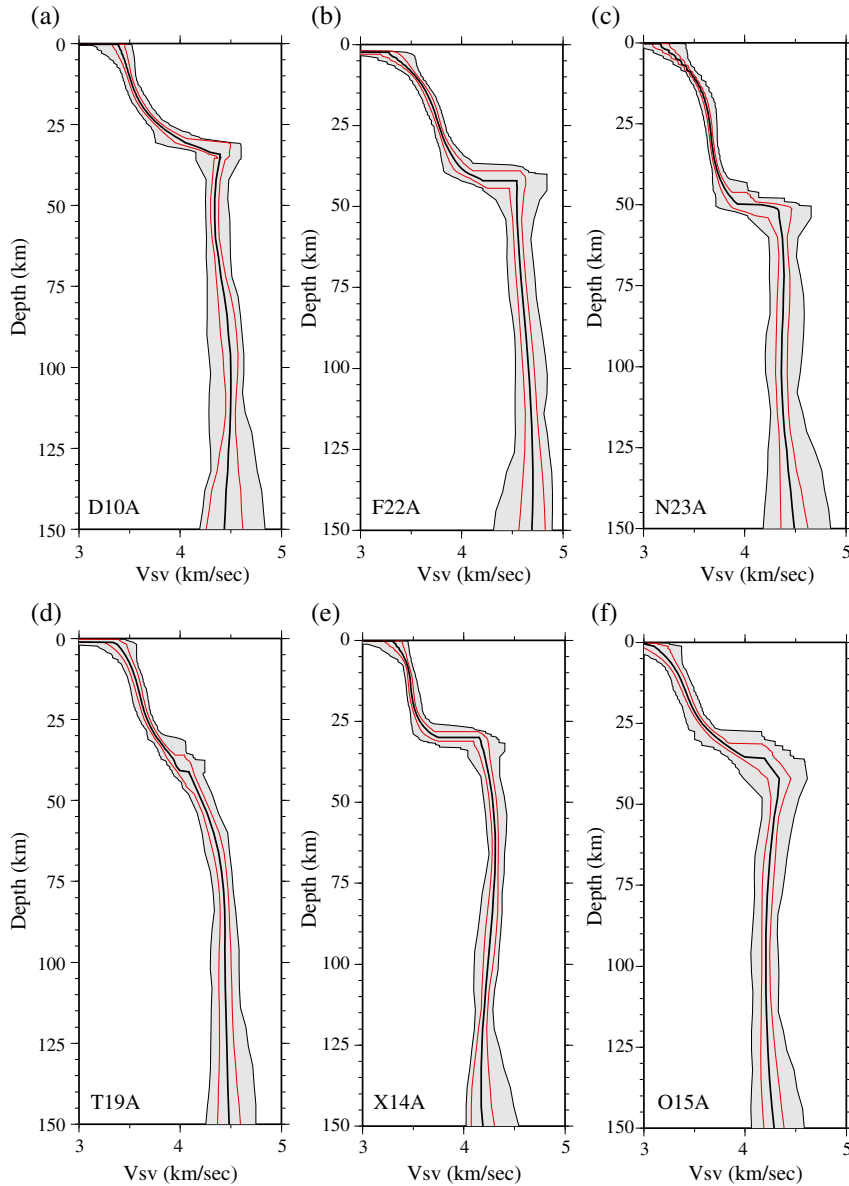
Figure 4. Six examples of azimuthally independent receiver functions (pair of black lines) and Rayleigh wave phase speed curves (error bars) compared with predictions from the best fitting model from the joint inversion (red lines) found in Figure 5. (a) TA station D10A, Oakesdale, WA (47.05, −117.28). (b) Station F22A, Rosebud, MT (45.78, −106.26). (c) Station N23A, Red Feather Lakes, CO (40.89, −105.94). (d) Station T19A, Beclabito, NM (36.83, −109.02). (e) Station X14A, Yava, AR (34.47, −112.89). (f) Station O15A, Rush Valley, UT (40.28, −112.47).

wave reduced chi-squared value less than unity for the best fitting model in the accepted ensemble: $\chi^2_{min} < 1$.

[17] Receiver functions are also usually well fit in the joint inversion such that 92% of the stations have a best fitting reduced chi-squared value $\chi^2_{min} < 1$ for the receiver function. Receiver function misfits (reduced square root of chi-squared) from the jointly best fitting model at each location are presented in Figure 6b. The stations with larger receiver function misfits are principally in California. This is largely due to differential resolution between the receiver function and surface wave data, particularly the sensitivity of the receiver function to relatively small-scale sedimentary basins,

which are not reflected in the surface wave data. An example of this is shown in Figures 7a–7c for a point in the Salton Trough in southern California. The receiver function (Figure 7b) from 0–4 s shows clear effects of deep sediments that are unfit by the receiver function predicted from the best fitting model. In contrast, phase velocities at this location (Figure 7c) do not display the low velocities at the short period end of the measurement band that are characteristic of the presence of sediments. At this point in the Salton Trough, the best fitting model fits the phase velocities exceptionally well and the receiver function much more poorly. Nevertheless, the observed receiver function at

Figure 5. The ensembles of accepted models (defined as in Figures 2c and 2d) from the joint inversion determined from the corresponding pairs of receiver functions and Rayleigh wave phase speed curves found in Figure 4.
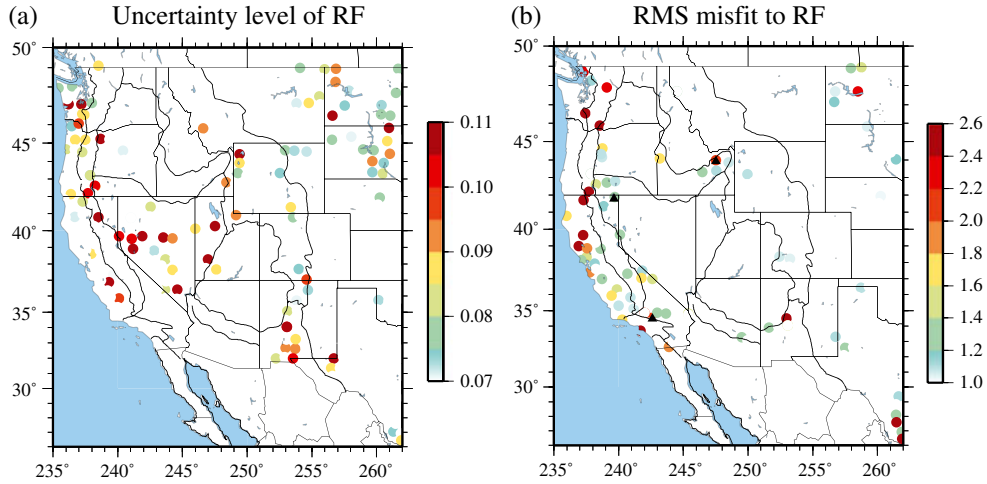
times greater than 4 s is fit, meaning that it provides useful constraints on structures deeper in the crust.

[18] Another example of a station where the receiver function is poorly fit is presented in Figures 7d–7f for a point in the northeastern Snake River Plain. In this case, although the receiver function (Figure 7e) is not fit well, it is fit better than the receiver function in Figure 6b. However, the price is that the phase velocity data are not as well fit here. Again, this is a differential resolution problem in which the receiver function and surface wave data reflect different structures.
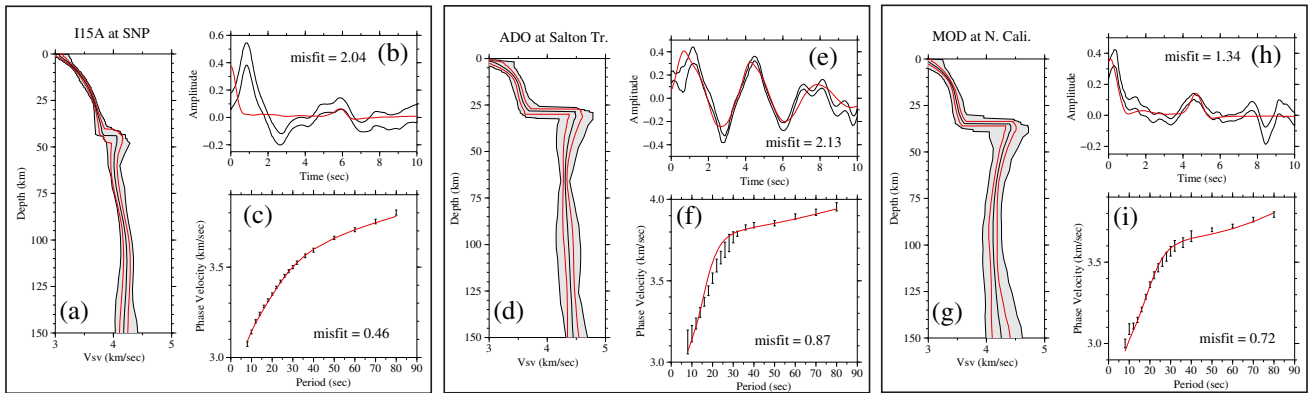
[19] A final example of a receiver function in Northern California that is not well fit in the inversion is presented in Figures 7g–7i. This is an example of the effect of mis-parameterization, where the real earth possesses a structure that cannot be represented by the specified parameterization. The receiver function (Figure 7h) shows an arrival near 8.5 s

presumably caused by a discontinuity or discontinuities in the uppermost mantle, which the smooth parameterization cannot reproduce. The phase velocity data also show the need for higher velocities in the uppermost mantle at periods between 50 and 70 s. However, the receiver function is well fit at times before 6 s, meaning that crustal structures are unaffected by the mantle mis-parameterization. Issues like this can be resolved in a later round of model production by re-parameterizing the model.

[20] As discussed by *Shen et al.* [2013], more complicated Moho structure such as the imbricated Moho identified by *Hansen and Dueker* [2009] across the Cheyenne Belt in Wyoming would also not be modeled with our parameterization. The station spacing of the TA largely avoids the regions of the Cheyenne Belt with particularly distinct double Moho, however.

Figure 6. (a) The time-averaged uncertainty in the receiver function for each station is plotted across the region of study. Receiver function uncertainty is defined as the half width of the receiver function corridor shown, for example, in Figures 2b and 4. Values greater than 0.07 are considered large. (b) Misfit to the receiver function from the best fitting model in the joint inversion is plotted. Misfit is defined as the square root of the reduced chi-squared value and referred to as χ_{min}. Black triangles are the locations of stations I15A, ADO, and MOD presented in Figure 7.

Figure 7. The three panels present examples of the joint inversion where the (b, e, h) receiver functions are poorly fit for stations in the Snake River Plain (I15A, SNP), the Salton Trough (ADO), and northern California (MOD). Station locations are presented in Figure 6b. (a, d, and g) The ensemble of accepted models for each location. (c, f, and i) Fit to the local Rayleigh wave dispersion curves. Formats of all plots are defined in Figure 2.
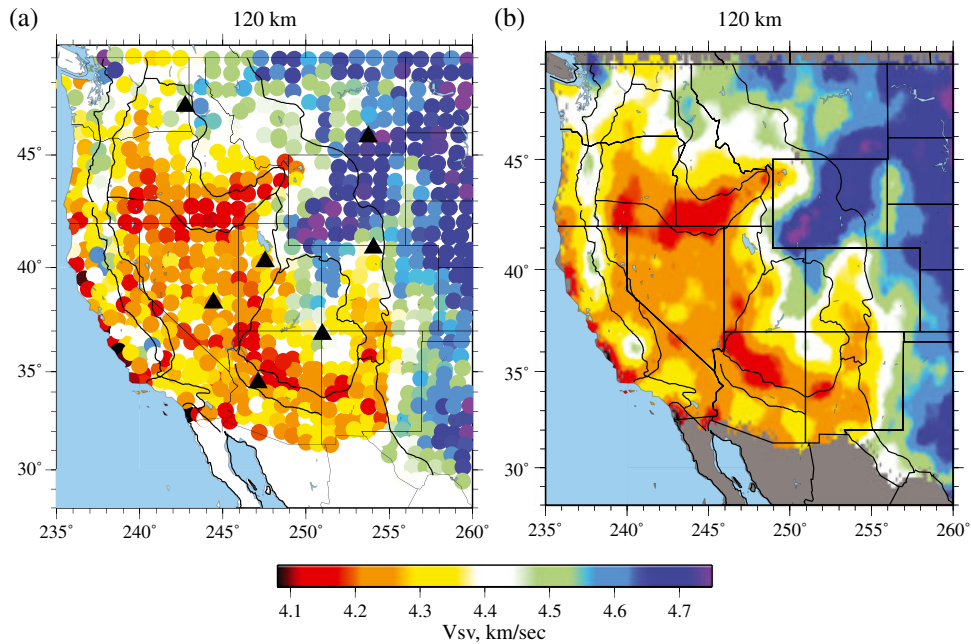
3. Discussion

[21] The joint inversion is performed at the locations of the TA stations, producing an irregularly spaced mosaic of distributions of 1-D models separated, on average, by about 70 km. An example for the model at 120 km depth is shown in Figure 8a. At each depth, simple kriging guided by model uncertainties [e.g., *Schultz et al.*, 1998] is applied to interpolate the models onto a $0.25° \times 0.25°$ grid as seen in Figure 8b. Views of averages of the distributions of accepted models are presented in Figures 8b, 9, 10, and 11.

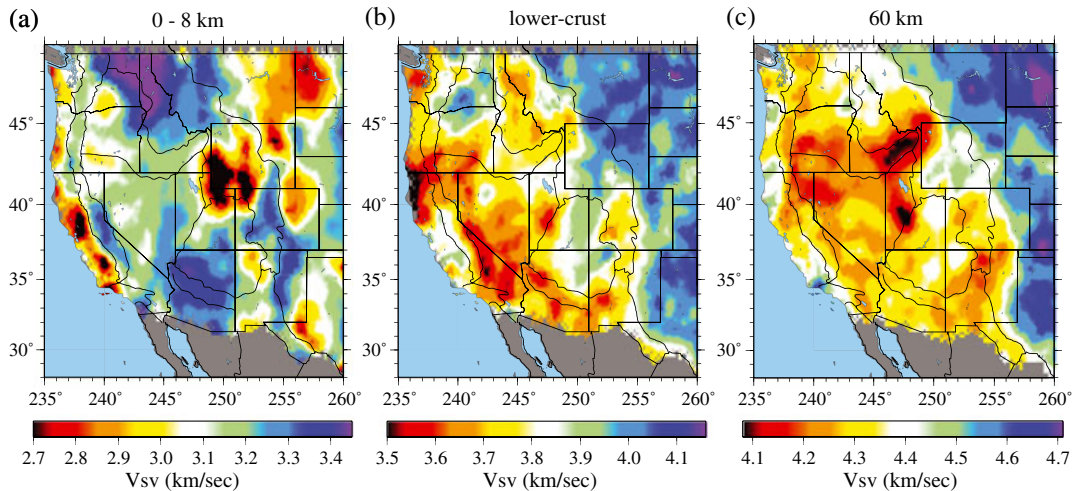### 3.1. Features of the 3-D Model

[22] The upper crustal part of the model is dominated by the existence or absence of sediments. The low-velocity features in Figure 9a are located at the major sedimentary basins of the central and Western US, including the Central (or Great) Valley of California, the Pasco basin in Washington, most prominently the Wyoming-Utah-Idaho thrust belt covering southwestern Wyoming, the Powder River basin in northeast Wyoming, the Williston basin in North Dakota and eastern Montana, the Denver basin in northeast Colorado, and parts of the Permian and Anadarko basins near the edge of the map in Texas. The velocity anomaly of the Pasco basin is weaker than the others because of capping or interlayering of sediments by basalt flows. The sedimentary parameterization in the model is quite simple, and inaccuracies in the resulting sedimentary model may cause low velocities to leak into the upper crystalline crust but no deeper. Although sediments are not prominent features of the vertical profiles presented in

Figure 8. (a) Average of Vsv from the distribution of accepted models from the joint inversion in the depth range from 105 to 135 km, presented as a mosaic of results at each station location. Black triangles are station locations for results in Figures 3–5. (b) The same as Figure 8a, but wave speeds have been interpolated onto a 0.25° × 0.25° grid by simple kriging, in which model uncertainties guide the interpolation.
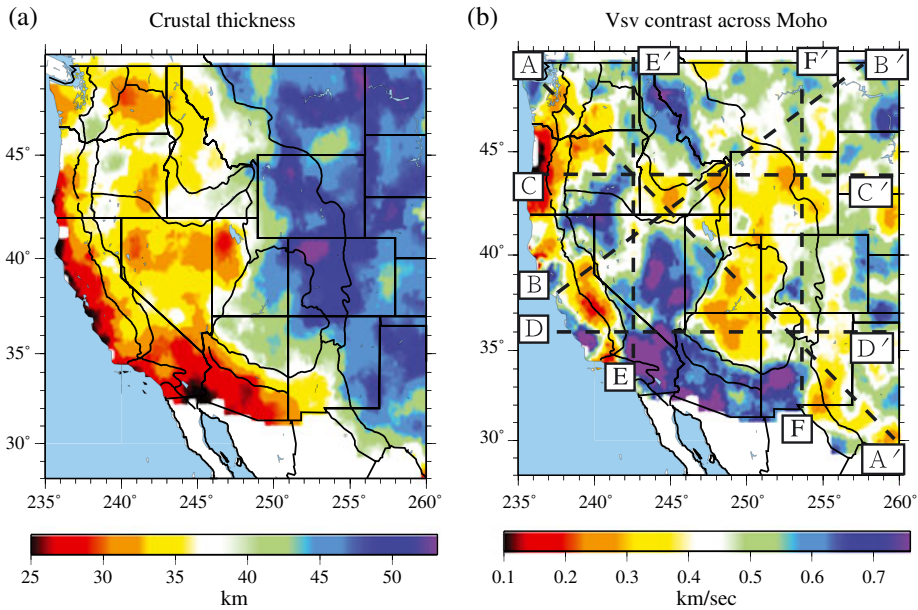

Figure 9. Average of Vsv from the distribution of accepted models from the joint inversion at three depths. (a) Average of the model between 0 and 8 km depth, (b) average of the model in the lower 4 km of the crust above Moho, and (c) the average of the model in the depth range between 50 and 70 km.
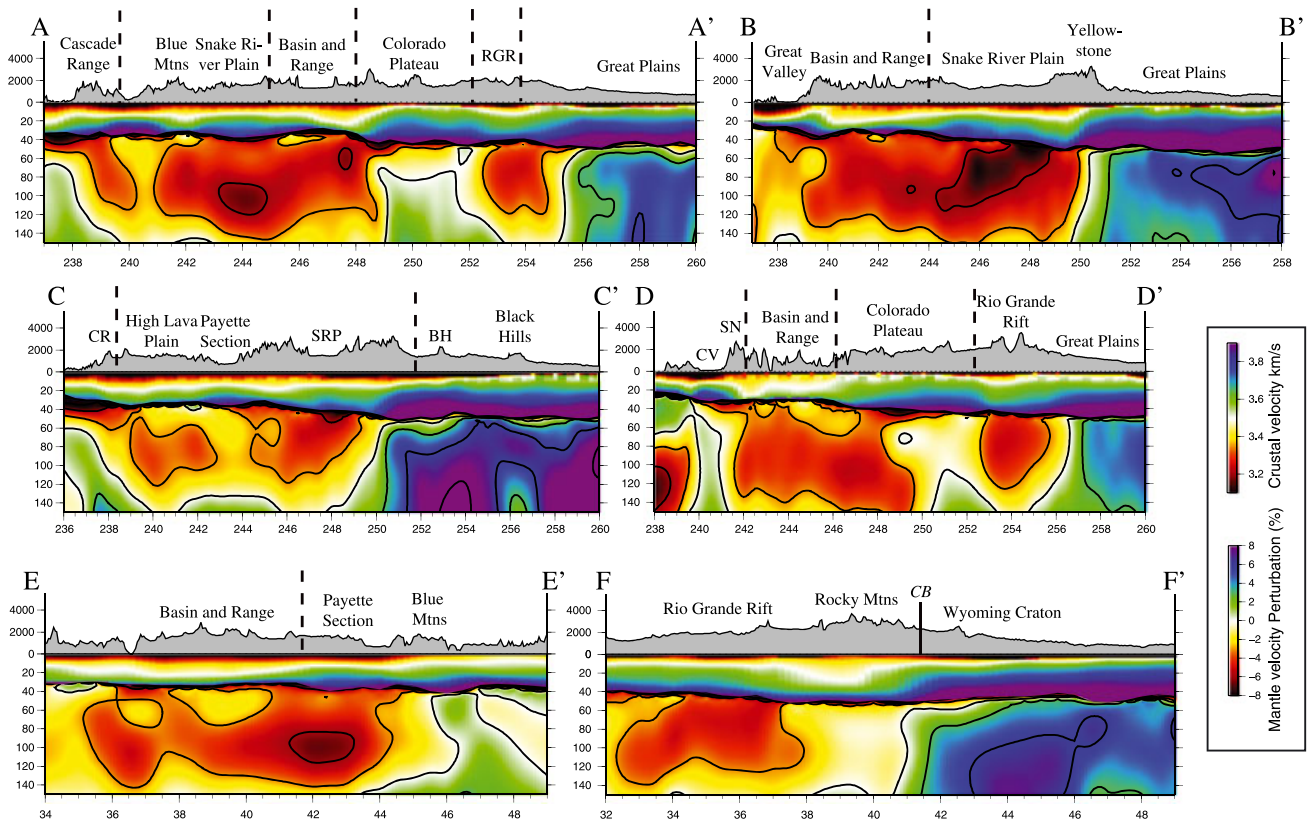
Figure 11, they do appear clearly beneath the Great (or Central) Valley of California in profiles B-B′ and D-D′. High upper crustal velocities in Figure 9a, reflecting the lack of sediments, are correlated principally with extrusive volcanism (e.g., Columbia Plateau) or mountain ranges; e.g., the Rocky Mountain cordillera, the Colorado Plateau, the eastern and southern Basin and Range province, and the Sierra Nevada.

[23] The predominant large-scale feature that appears in the lower crust (Figure 9b) is the dichotomy between the high shear wave speeds in the Great Plains east of the Rocky Mountain front and the generally lower wave speeds in the tectonically deformed west. High lower crustal velocities in the west are associated with Pasco basin intrusives of the Columbia River flood basalt province, the Wyoming craton, and the interior (particular the northern interior) of the Colorado Plateau. Relative high velocities are found beneath the Snake River Plain. Midcrustal velocities are higher relative to surroundings than lower crustal velocities. These

Figure 10. Average of (a) crustal thickness and (b) the jump in Vsv across the Moho from the ensemble of accepted models derived from the joint inversion. Vertical model profiles that are plotted in Figure 11 are identified in Figure 10b.

Figure 11. Vertical Vsv model profiles for the six transects identified in Figure 10b with dashed lines. Speeds in the crust are in absolute units, and those in the mantle are presented as percent perturbations relative 4.4 km/s, except along profile C-C′ where it is 4.32 km/s. Mantle velocity contours appear at 3% intervals. RGR, Rio Grande Rift; CR, Cascade Range; SRP, Snake River Plain; BH, Bighorn Range; CV, Central Valley; SN, Sierra Nevada; CB, Cheyenne Belt.

high lower crustal velocities in the Western US may be compositional in origin, reflecting either past volcanism or the presence of Archean cratonic blocks. A likely cause for fast lower crust under the Columbia Plateau and Snake River Plain is a mafic underplate associated with basaltic magmatism. Low velocities in the lower crust are found prominently in the southern Basin and Range province, on the western and southern peripheries of the Colorado Plateau, and in coastal California north of Cape Mendocino near the southern end of the subducting Gorda plate. Fast lower crustal velocities appear conspicuously in the Great Plains on the vertical profiles of Figure 11 but also strikingly beneath the Colorado Plateau (A-A′, D-D′). The persistence of high-velocity, presumably strong lower crust under the Laramide-affected Wyoming craton and the Colorado Plateau suggests that crustal strength may influence surface deformation. In contrast, the lower crustal velocity contrast tracking the Rocky Mountain deformation front and Rio Grande Rift truncates much older Proterozoic mafic lower crust (the "7.xx layer" seen by *Gorman et al.* [2002] in Wyoming and Montana and the granite-rhyolite province lower crustal restite proposed by *Karlstrom et al.* [2005] to the east and cuts across the general NE-SW trend inherited from continental assembly [*Whitmeyer and Karlstrom*, 2007].

[24] Crustal thickness and the jump in shear velocity across the Moho, two of the variables most improved by the introduction of receiver function waveforms in the inversion, are presented in Figures 10a and 10b. To first order, crustal thickness agrees with similar estimates made by *Gilbert* [2012] using receiver functions alone, except in regions where the Moho converted arrival, which provides information about crustal thickness, is of very low amplitude or absent, such as beneath parts of the Colorado Plateau (Figures 4d and 5d). The thickest crust is in the northern Colorado Rockies (~60 km), consistent with the regional receiver function analysis of *Karlstrom et al.* [2012] using a denser array. Thinnest crust is less than 25 km in the Salton Trough. Even across the Great Plains, crustal thickness varies appreciably from about 42 km depth in northern Nebraska to about 55 km near the Montana-North Dakota border. Another example of thinned crust is observed near the boundary of Wyoming and Montana, which was also observed by *Gilbert* [2012].

[25] Crustal thickness is not simply related to surface elevation; for example, there is little obvious difference between the crustal thicknesses near the Rocky Mountain front with the Great Plains. The 3-D model presented here, however, is the basis for the prediction of surface elevation from derived density variations within the crust and uppermost mantle [e.g., *Levandowski et al.*, 2012]. It is found that isostatic surface topography predicted from density variations derived from this 3-D Vs model generally fits the observed topography across the Western US, and the exceptions are informative.

[26] Regions that have a low amplitude for the Moho converted arrival in the receiver function appear in Figure 10b as small jumps in Vs across Moho and are presented with warm colors. These regions include parts of the coastal Pacific Northwest of Oregon, the Sierra Nevada, the Snake River Plain, parts of Wyoming, and the Colorado Plateau. A relationship to lithospheric delaminations or mantle drips is possible, as proposed in the Southern Sierra Nevada [*Zandt*

et al., 2004, *Boyd et al.*, 2004] and the Colorado Plateau [*Levander et al.*, 2011; *Bailey et al.*, 2012], which are underlain by relatively fast uppermost mantle. However, a reduced Moho velocity contrast is also consistent with high-velocity lower crust, such as an eclogitic root under the western Sierra Nevada foothills [*Frassetto et al.*, 2011] or a mafic underplate. Most of the Basin and Range province has a large contrast in Vs across the Moho, as do parts of the Rocky Mountains and the Great Plains. The reduced contrast in Vs across the Moho west of the Cascade Range in the Pacific Northwest contains the region hypothesized to have serpentinized uppermost mantle [e.g., *Bostock et al.*, 2002; *Brocher et al.*, 2003].

[27] Low mantle velocities (Figures 8 and 9c) are generally correlated with lower crustal velocities across the region probably because of the continuity of thermal anomalies across the Moho. Principal exceptions are the Pasco basin in southern Washington, the Snake River Plain, and the southwestern Basin and Range adjacent to the Sierra Nevada (Walker Lane), perhaps indicative of compositional heterogeneity in the crust caused by fast volcanic intrusives overlying slow hot mantle. The model in the mantle is resolved to scales of geological and tectonic relevance, and many features are observed on the vertical profiles of Figure 11 that are deserving of further detailed analysis and thermal modeling.

[28] Examples on profile A-A′ include the observation of low velocities in the supra-slab wedge beneath the Cascade Range, the Snake River Plain, the Basin and Range Province, and the Rio Grande Rift as well as high velocities beneath the Colorado Plateau. On profile B-B′, the along hot spot track tilt of the low-velocity anomaly underlying the Snake River Plain is seen as well as the rapid transition to high velocities beneath the Great Plains. The subducting Juan de Fuca slab appears on profile C-C′ along with a resolved deep relative low-velocity feature underlying the Black Hills of South Dakota. It is interesting and enigmatic that the Black Hills mantle anomaly is exclusively deep in the model. The mantle drip [*Boyd et al.*, 2004; *Zandt et al.*, 2004; *Yang and Forsyth*, 2006] underlying the Central Valley of California and the western Sierra Nevada is seen in profile D-D′, along with low velocities beneath the Rio Grande Rift and the rapid transition to the Great Plains province in eastern New Mexico, which is consistent with previous studies [*Wilson et al.*, 2005; *Gao et al.*, 2004; *West et al.*, 2004]. The eastward down-tilted low anomaly beneath the Basin and Range/western Colorado Plateau viewed in profile D-D′ may be related to the complex embedment of the previous flat-subducted Farallon slab. The thin lithosphere observed beneath the Colorado Plateau in profiles A-A′ and D-D′ is consistent with earlier observations by *Levander et al.* [2011] and *Bailey et al.* [2012]. Profile E-E′ presents a south-north transect of the Basin and Range province illustrating relatively higher velocities directly underlying Moho that characterize parts of this province. Higher velocities underlie the Blue Mountains, consistent with body wave tomography [*Hales et al.*, 2005] and dip northward with increasing depth. Finally, profile F-F′ presents a south-north transect of the Rio Grande Rift and Rocky Mountains, illustrating the much lower shear wave speeds underlying the rift, and the rapid transition to high-velocity mantle across the Cheyenne belt at the edge of the Archean Wyoming craton. The high velocities present in the lower crust of the Wyoming Craton in profile F-F′ may diagnose the "double Moho" north of the Cheyenne
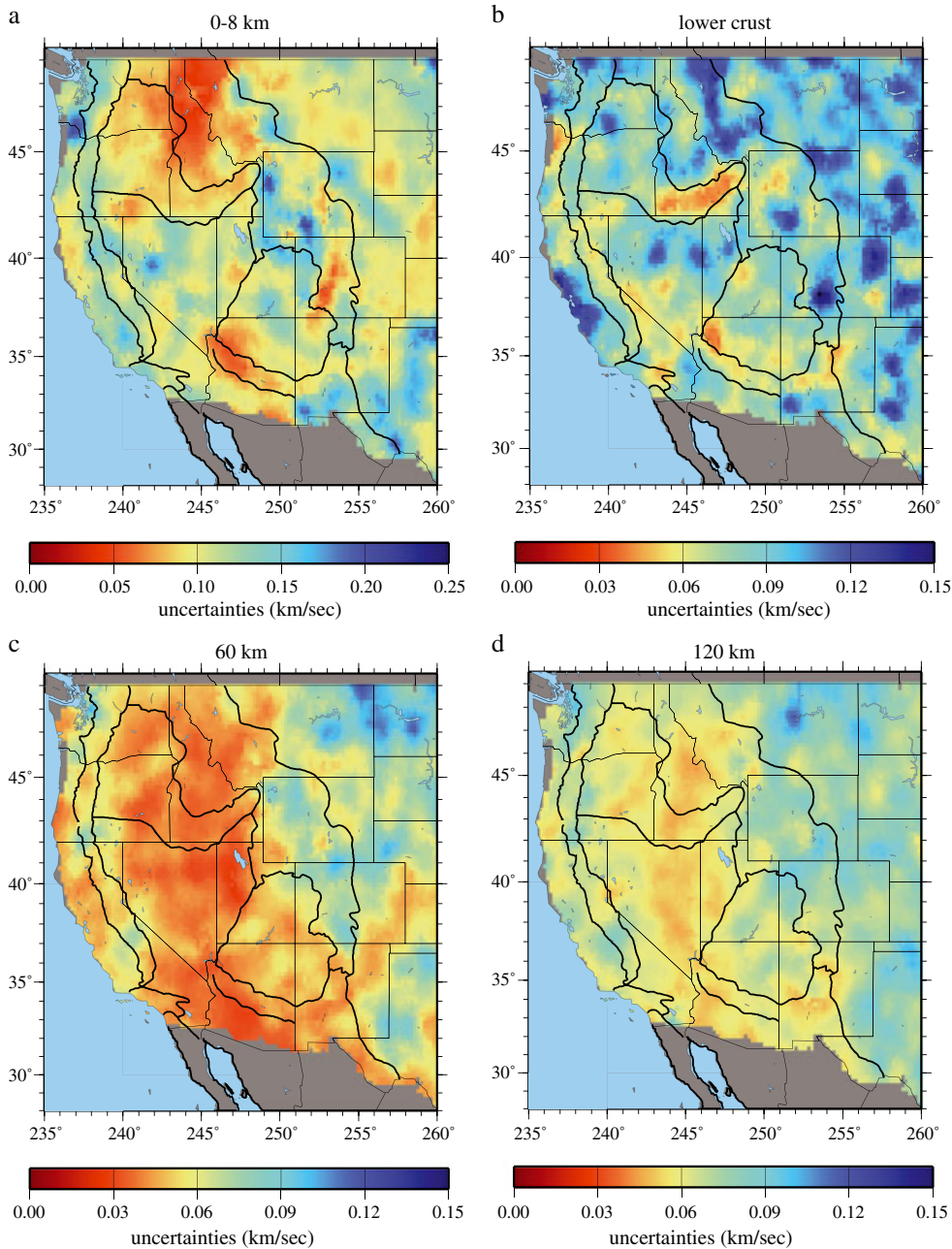
Belt, which has been argued to result from underplating based on previous refraction studies [e.g., *Gorman et al.*, 2002; *Rumpfhuber et al.*, 2009; *Rumpfhuber and Keller*, 2009].

[29] On average, the uppermost mantle structure is similar to previous models in the overlapping area [*Yang et al.*, 2008; *Moschetti et al.*, 2010a, 2010b] and is also similar to models constructed from surface wave/body wave tomography by *Schmandt and Humphreys* [2010] and *Obrebski et al.* [2011]. However, the assimilation of receiver functions greatly improves the vertical resolution in the top 100 km of the model, whereas body wave tomography reveals much deeper structure.
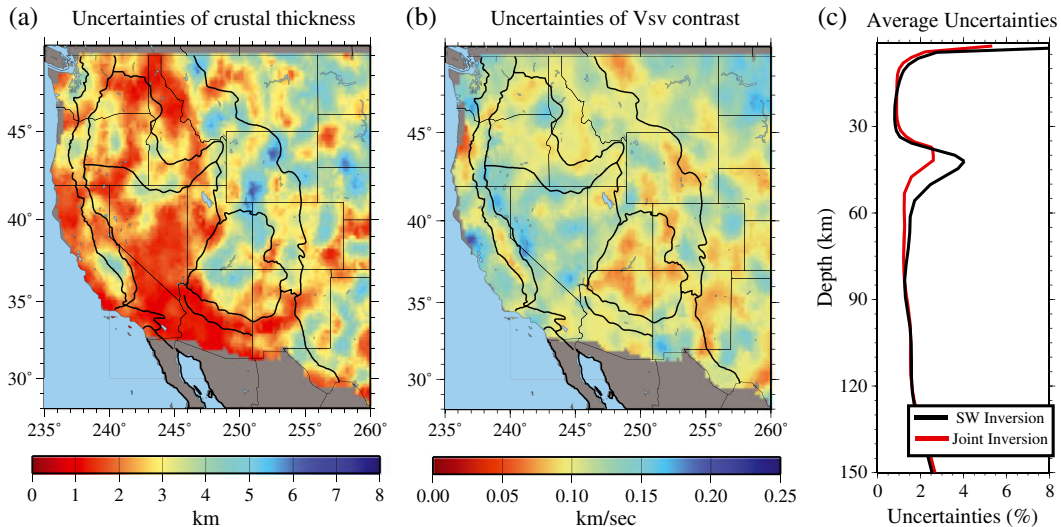
3.2. Model Uncertainties

[30] One of the advantages of the Bayesian Monte Carlo method is that it provides uncertainties in the final model, determined from the standard deviation of the resulting marginal posterior distribution at each depth. Figures 8, 9, 10, and 11 present averages of the distributions at each depth, examples of which are shown in Figures 3d–3f. Figures 12 and 13 summarize the uncertainties at the depths and for crustal thickness and Vs jump across Moho shown in Figures 8, 9, and 10. Uncertainties in the upper crust average about 100 m/s, with larger values near the Wyoming basins (150–200 m/s) due to the complexity of sedimentary

Figure 12. Estimates of uncertainties (1σ) in the 3-D model at three four depths: (a) 0–8 km average, (b) lower crustal average (4 km above Moho to Moho), (c) 60 km, and (d) 120 km.

Figure 13. Estimates of uncertainty (1σ) for (a) estimated crustal thickness and (b) the jump in shear wave speed across the Moho. (c) Model uncertainties (1σ) averaged over the study region from the inversion with surface wave (SW) data alone (black line) and from the joint inversion (red line).

structure there. Uncertainties also grow near the periphery of the maps because surface wave dispersion uncertainties increase there. In the lower crust, uncertainties are slightly smaller than in the upper crust but are still substantial due to remaining trade-offs with Moho depth and uppermost mantle velocities. The pattern of uncertainties at this depth (Figure 12b), therefore, is correlated with the uncertainties in crustal thickness (Figure 13a). At 60 km depth, uncertainties are much smaller than in the upper and lower crust, about 50 m/s across much of the region, because this depth is separated from structural discontinuities across most of the region. In regions with thick crust, however, uncertainties increase to about 100 m/s. At 120 km depth, uncertainties increase again because the structural sensitivity of surface waves decays with depth.

[31] Figure 13c presents the spatial average of the standard deviation of these distributions across the study region for both the joint inversion and the inversion with surface wave data alone. The introduction of receiver functions reduces model uncertainties predominantly between depths of 35 and 50 km, by introducing information about the depth to Moho and the velocity contrast across it. This uncertainty, represented as the spread of the distribution, however, does not include bias. In fact, relative to the earlier studies of *Yang et al.* [2008] and *Moschetti et al.* [2010a, 2010b], the improvements actually extend to greater depths because to reduce the spread of models near Moho those studies imposed a positivity constraint on the velocity derivative with depth, which is not needed in the joint inversion. In some locations, that constraint obscured the location in depth of the mantle anomalies, and its removal further improves the vertical resolution of the model.

4. Conclusions

[32] The joint analysis of surface waves from ambient noise and earthquake data produces high resolution (~70 km)

Rayleigh wave dispersion maps from about 8 to 80 s period. Finite frequency effects should be accounted for at periods above about 40 s [*Lin and Ritzwoller*, 2011b] and are effected here through Helmholtz tomography [*Lin and Ritzwoller*, 2011a]. Eikonal tomography (applied to ambient noise data) and Helmholtz tomography (applied to earthquake data) provide the uncertainty information needed to interpret the signals in ambient noise and earthquake maps quantitatively and reliably. In the frequency band of overlap between ambient noise and earthquake data, the ambient noise and earthquake-derived phase velocity maps agree remarkably well.

[33] Bayesian Monte Carlo inversions of the surface wave dispersion data alone reveal that shear wave speeds at depths well separated from first-order discontinuities (base of sediments, Moho) are well recovered by surface wave data alone. Near the discontinuities, however, trade-offs between the interface depths and adjacent shear wave speeds spread the ensemble of accepted models. Ad hoc constraints introduced to reduce such trade-offs have other deleterious effects, such as causing mantle anomalies to move to different depths. The assimilation of receiver functions into the joint inversion with Rayleigh wave dispersion curves overcomes these difficulties, improving the vertical resolution of the model by reducing the range of estimated Moho depths, improving the determination of the shear velocity jump across Moho, and improving the resolution of the depth of anomalies in the uppermost mantle. The joint inversion produces a distribution of models beneath each station, which is summarized by the mean and standard deviation of the distribution at each depth. Across the vast majority of the region studied, the surface wave dispersion and receiver functions can be fit jointly with a very simple model parameterization, producing a smooth model between the two internal discontinuities. There are, however, details in the receiver functions, signals arriving more than 10 s after the direct *P*-arrival, as well as azimuthal variations in the receiver functions that call for further refinement of the models

with structures at greater depths or with local 2-D structures and anisotropy. But these features are beyond the scope of the present study.

[34] A great variety of geological and tectonic features are revealed in the 3-D model presented here that forms the basis for more detailed local to regional scale analysis and interpretation in the future.

[35] The 3-D model is useful as a basis for many other types of studies: studies of azimuthally/radially anisotropic structures, investigations of the density/thermal structure of the study region, and as a starting model for other types of seismic investigations such as Common-Conversion Point stacking and body wave tomography [e.g., *Obrebski et al.*, 2011]. In addition, the 3-D model can be used to improve regional seismic event location based on short period surface waves, examples of which have been discussed by *Barmin et al.* [2011] and *Levshin et al.* [2012].

References

Bailey, I. W., M. S. Miller, K. J. Liu, and A. Levander (2012), V-S and density structure beneath the Colorado Plateau constrained by gravity anomalies and joint inversions of receiver function and phase velocity data, *J. Geophys. Res.*, 117, B02313, doi:10.1029/2011JB008522.

Barmin, M. P., A. L. Levshin, Y. Yang, and M. H. Ritzwoller (2011), Epicentral location based on Rayleigh wave empirical Green's functions from ambient seismic noise, *Geophys. J. Int.*, 184(2), 869–884.

Bensen, G. D., M. H. Ritzwoller, M. P. Barmin, A. L. Levshin, F. Lin, M. P. Moschetti, N. M. Shapiro, and Y. Yang (2007), Processing seismic ambient noise data to obtain reliable broad-band surface wave dispersion measurements, *Geophys. J. Int.*, 169(3), 1239–1260, doi:10.1111/j.1365-246X.2007.03374.x.

Bensen, G. D., M. H. Ritzwoller, and N. M. Shapiro (2008), Broad-band ambient noise surface wave tomography across the United States, *J. Geophys. Res.*, 113, B05306, doi:10.1029/2007JB005248.

Bianchi, I., J. Park, N. Piana Agostinetti, and V. Levin (2010), Mapping seismic anisotropy using harmonic decomposition of receiver functions: An application to Northern Apennines, Italy, *J. Geophys. Res.*, 115, B12317, doi:10.1029/2009JB007061.

Bodin, T., M. Sambridge, H. Tkalčić, P. Arroucau, K. Gallagher, and N. Rawlinson (2012), Transdimensional inversion of receiver functions and surface wave dispersion, *J. Geophys. Res.*, 117, B02301, doi:10.1029/2011JB008560.

Bostock, M. G., R. D. Hyndman, S. Rondenay, and S. M. Peacock (2002), An inverted continental Moho and serpentinization of the forearc mantle, *Nature*, 417, 536–538.

Boyd, O. S., C. H. Jones, and A. F. Sheehan (2004), Foundering lithosphere imaged beneath the Southern Sierra Nevada, California, USA, *Science*, 305, 660–662.

Brocher, T. M. (2005), Empirical relations between elastic wavespeeds and density in the Earth's crust, *Bull. Seism. Soc. Am.*, 95, 2081–2092, doi:10.1785.0120050077.

Brocher, T. M. (2008), Compressional and shear-wave velocity versus depth relations for common rock types in Northern California, *Bull. Seism. Soc Am.*, 98(2), 950–968, doi:10.1785/0120060403.

Brocher, T. M., T. Parsons, A. M. Tréhu, C. M. Snelson, and M. A. Fisher (2003), Seismic evidence for widespread serpentinized forearc upper mantle along the Cascadia margin, *Geology*, 31, no. 3, 267–270.

Christensen, N. I., and W. D. Mooney (1995), Seismic velocity structure and composition of the continental crust: A global view, *J. Geophys. Res.*, 100(B6): 9761–9788.

Chang, S. J., C. E. Baag, and C. A. Langston (2004), Joint analysis of teleseismic receiver functions and surface wave dispersion using the genetic algorithm, *Bull. Seismol. Soc. Am.*, 94, 691–704.

Dziewonski, A., and D. Anderson (1981), Preliminary reference Earth model, *Phys. Earth Planet. Int.*, 25(4): 297–356.

Frassetto, A. M., G. Zandt, H. Gilbert, T. J. Owens, and C. H. Jones (2011), Structure of the Sierra Nevada from receiver functions and implications for lithospheric foundering, *Geosphere*, 7, 898–921.

Gao, W., S. P. Grand, W. S. Baldridge, D. Wilson, M. West, J. F. Ni, and R. Aster (2004), Upper mantle convection beneath the central Rio Grande rift imaged by *P* and *S* wave tomography, *J. Geophys. Res-Solid Earth*, 109, 16.

Girardin, N., and V. Farra (1998), Azimuthal anisotropy in the upper mantle from observations of *P*-to-*S* converted phases: Application to southeast Australia, *Geophys. J. Int.*, 133, 615–629.

Gilbert, H. (2012), Crustal structure and signatures of recent tectonism as influenced by ancient terranes in the Western United States, *Geosphere*, 8, 141–157, doi:10.1130/GES00720.1.

Gorman, A. R., R. M. Clowes, R. M. Ellis, T. J. Henstock, G. D. Spence, G. R. Keller, A. Levander, C. M. Snelson, M. J. A. Burianyk, E. R. Kanasewich, I. Asudeh, Z. Hajnal, and K. C. Miller (2002), Deep probe: Imaging the roots of western North America, *Can. J. Earth Sci.*, 39, 375–398.

Hales, T. C., D. L. Abt, E. D. Humphreys, and J. J. Roering (2005), A lithospheric instability origin for Columbia River flood basalts and Wallowa Mountains uplift in northeast Oregon, *Nature*, 438, 842–845.

Hansen, S., and K. Dueker (2009), *P*- and *S*-wave receiver function images of crustal imbrication beneath the Cheyene Belt of southeast Wyoming, *Bull. Seism. Soc. Am.*, 99, 1953–1961, doi:10.1785/0120080168.

Jones, C. H., and R. A. Phinney (1998), Seismic structure of the lithosphere from teleseismic converted arrivals observed at small arrays in the southern Sierra Nevada and vicinity, California, *J. Geophys. Res.*, 103(B5), 10,065–10,090, doi:10.1029/97JB03540.

Julia, J., C. J. Ammon, R. B. Herrmann, and A. M. Correig (2000), Joint inversion of receiver function and surface wave dispersion observations, *Geophys. J. Int.*, 143, 99–112.

Kanamori, H., and D. Anderson (1977), Importance of physical dispersion in surface wave and free oscillation problems: Review, *Revs. Geophys. Space Phys.*, 15(1):105–112.

Karato, S. (1993), Importance of anelasticity in the interpretation of seismic tomography, *Geophys. Res. Lett.*, 20(15), 1623–1626, doi:10.1029/93GL01767.

Karlstrom, K. E., S. J. Whitmeyer, K. Dueker, M. L Williams, S. Bowring, A. Levander, E. D. Humphreys, G. R. Keller, and CR-Rom Working Group (2005), Synthesis of results from the CD-ROM experiment: 4-D image of the lithosphere beneath the Rocky Mountains and implications for understanding the evolution of continental lithosphere, in: Karlstrom, K. E., and Keller, G. R., eds. The Rocky Mountain region—an evolving lithosphere. AGU Geophysical Monograph, 154, doi:10:1029/154GM31.

Karlstrom, K. E., D. Coblentz, K. Dueker, W. Ouimet, E. Kirby, J. Van Wijk, B. Schmandt, S. Kelley, G. Lazear, L. J. Crossey, R. Crow, A. Aslan, A. Darling, R. Aster, J. MacCarthy, S. M. Hansen, J. Stachnik, D. F. Stockli, R. V. Garcia, M. Hoffman, R. McKeon, J. Feldman, M. Heizler, M. S. Donahue, and C. W. Grp (2012), Mantle-driven dynamic uplift of the Rocky Mountains and Colorado Plateau and its surface response: Toward a unified hypothesis, *Lithosphere*, 4, 3–22.

Langston, C. A. (1979), Structure under Mount Rainier, Washington, inferred from teleseismic body waves, *J. Geophys. Res.*, 84(B9), 4749–4762, doi:10.1029/JB084iB09p04749.

Last, R. J., A. A. Nyblade, C. A. Langston, and T. J. Owens (1997), Crustal structure of the East African Plateau from receiver functions and Rayleigh wave phase velocities, *J. Geophys. Res.*, 102(B11), 24,469–24,483, doi:10.1029/97JB02156.

Lawrence, J. F., and D. A. Wiens, (2004), Combined receiver-function and surface wave phase-velocity inversion using a niching genetic algorithm: Application to Patagonia, *Bull. Seismol. Soc. Am.*, 94, 977–987.

Levander, A., B. Schmandt, M. S. Miller, K. Liu, K. E. Karlstrom, R. S. Crow, C. T. A. Lee, and E. D. Humphreys (2011), Continuing Colorado plateau uplift by delamination-style convective lithospheric downwelling, *Nature*, 472, 461–U540.

Levandowski, W. B., C. H. Jones, W. Shen, M. Ritzwoller, and V. Schulte-Pelkum (2012), Why what's where in the West: Density, buoyancy and gravitational potential energy, *EOS Trans. AGU*, 93, Fall Meet. Suppl., abstract T21E-2627.

Ligorria, J. P., and C. J. Ammon (1999), Iterative deconvolution and receiver-function estimation, *Bull. Seismol. Soc. Am.*, 89(5), 1395–1400.

Levshin, A. L., M. P. Barmin, M. P. Moschetti, C. Mendoza, and M. H. Ritzwoller (2012), Refinements to the method of epicentral location based on surface waves from ambient seismic noise: Introducing Love waves, *Geophys. J. Int.*, 191(2), 671–685, doi:1111/j.1365.246x.2012.05631.x.

Lin, F.-C., and M. H. Ritzwoller (2011a), Helmholtz surface wave tomography for isotropic and azimuthally anisotropic structure, *Geophys. J. Int.*, 186, (3), 1104–1120, doi:10.1111/j.1365-246X.2011.05070.x.

Lin, F.-C., and M. H. Ritzwoller (2011b), Apparent anisotropy in inhomogeneous isotropic media, *Geophys. J. Int.*, *186*(3), 1205–1219, doi:10.1111/j.1365-246X.2011.05100.x.

Lin, F.-C., M. P. Moschetti, and M. H. Ritzwoller (2008), Surface wave tomography of the Western United States from ambient seismic noise: Rayleigh and Love wave phase velocity maps, *Geophys. J. Int.*, *173*(1), 281–298, doi:10.1111/j.1365-246X.2008.03720.x.

Lin, F-C., M. H. Ritzwoller, and R. Snieder (2009), Eikonal tomography: Surface wave tomography by phase front tracking across a regional broad-band seismic array, *Geophys. J. Int.*, *177*(3), 1091–1110, doi:10.1111/j.1365-246X.2009.04105.x.

Lin, F.-C., M. H. Ritzwoller, Y. Yang, M. P. Moschetti, and M. J. Fouch (2010), Complex and variable crustal and uppermost mantle seismic anisotropy in the Western United States, *Nat. Geosci.*, *4*(1), 55–61, doi:10.1038/ngeo1036.

Liu, Q. Y., Y. Li, J. H. Chen, R. D. van der Hilst, B. A. Guo, J. Wang, S. H. Qi, and S. C. Li (2010), Joint inversion of receiver function and ambient noise based on Bayesian theory, *Chinese J. Geophys-Chinese Edn.*, *53*, 2603–2612.

Moschetti, M. P., M. H. Ritzwoller, and N. M. Shapiro (2007), Surface wave tomography of the Western United States from ambient seismic noise: Rayleigh wave group velocity maps, *Geochem. Geophys. Geosyst.*, *8*(8), 1–10, doi:10.1029/2007GC001655.

Moschetti, M. P., M. H. Ritzwoller, F. Lin, and Y. Yang (2010a), Seismic evidence for widespread western-US deep-crustal deformation caused by extension, *Nature*, *464*(7290), 885–9, doi:10.1038/nature08951.

Moschetti, M. P., M. H. Ritzwoller, F.-C. Lin, and Y. Yang (2010b), Crustal shear wave velocity structure of the Western United States inferred from ambient seismic noise and earthquake data, *J. Geophys. Res.*, *115*, B10, 1–20, doi:10.1029/2010JB007448.

Obrebski, M., R. M. Allen, F. Pollitz, and S. H. Hung (2011), Lithosphere-asthenosphere interaction beneath the Western United States from the joint inversion of body-wave traveltimes and surface-wave phase velocities, *Geophys. J. Int.*, *185*, 1003–1021.

Ozalaybey, S., M. K. Savage, A. F. Sheehan, J. N. Louie, and J. N. Brune (1997), Shear-wave velocity structure in the northern Basin and Range province from the combined analysis of receiver functions and surface waves, *Bull. Seismol. Soc. Am.*, *87*, 183–199.

Pollitz, F. F. (2008), Observations and interpretation of fundamental mode Rayleigh wavefields recorded by the Transportable Array (USArray), *Geophys. J. Int.*, *173*, 189–204.

Pollitz, F. F., and J. A. Snoke (2010), Rayleigh-wave phase-velocity maps and three-dimensional shear velocity structure of the Western US from local non-plane surface wave tomography, *Geophys. J. Int.*, *180*, 1153–1169.

Ritzwoller, M. H., F.-C. Lin, and W. Shen (2011), Ambient noise tomography with a large seismic array, *Comptes Rendus Geosci.*, *343*(8–9), 558–570, doi:10.1016/j.crte.2011.03.007.

Rumpfhuber, E.-M., and G. R. Keller (2009), An integrated analysis of controlled and passive source seismic data across an Archean-Proterozoic suture, *J. Geophys. Res.*, *114*, B08305, doi:10.1029/2008JB005886.

Rumpfhuber, E.-M., G. R. Keller, E. Sandvol, A. A. Velasco, and D. C. Wilson (2009), Rocky Mountain evolution: Tying continental dynamics of the Rocky Mountains and Deep Probe seismic experiments with receiver functions, *J. Geophys. Res.*, *114*, B08301, doi:10.1029/2008JB005726.

Schmandt, B., and E. Humphreys (2010), Complex subduction and small-scale convection revealed by body-wave tomography of the Western United States upper mantle, *Earth Planet. Sci. Lett.*, *297*, 435–445.

Schultz, C. A, S. C. Myers, J Hipp, and C. J. Young (1998), Nonstationary Bayesian kriging: A predictive technique to generate spatial corrections for seismic detection, location and identification, *Bull. Seism. Soc. Am. 88*, 1275–1288.

Shapiro, N. M., and M. H. Ritzwoller (2002), Monte-Carlo inversion for a global shear-velocity model of the crust and upper mantle, *Geophys. J. Int.*, *151*, 88–105.

Shapiro, N. M., M. Campillo, L. Stehly, and M. H. Ritzwoller (2005), High-resolution surface-wave tomography from ambient seismic noise, *Sci. (New York, N.Y.)*, *307*(5715), 1615–8, doi:10.1126/science.1108339.

Shen, W., M. H. Ritzwoller, V. Schulte-Pelkum, and F.-C. Lin (2013), Joint inversion of surface wave dispersion and receiver functions: A Bayesian Monte-Carlo approach, *Geophys. J. Int.*, doi:10.1093/gji/ggs050.

Tokam, A. P. K., C. T. Tabod, A. A. Nyblade, J. Julia, D. A. Wiens, and M. E. Pasyanos (2010), Structure of the crust beneath Cameroon, West Africa, from the joint inversion of Rayleigh wave group velocities and receiver functions, *Geophys. J. Int.*, *183*, 1061–1076.

West, M., J. Ni, W. S. Baldridge, D. Wilson, R. Aster, W. Gao, and S. Grand (2004), Crust and upper mantle shear wave structure of the southwest United States: Implications for rifting and support for high elevation, *J. Geophys. Res-Solid Earth*, *109*, 16.

Whitmeyer S. J., and K. E. Karlstrom (2007), Tectonic model for the Proterozoic growth of North America, *Geosphere*, *3*, 220–259.

Wilson, D., R. Aster, J. Ni, S. Grand, M. West, W. Gao, W. S. Baldridge, and S. Semken (2005), Imaging the seismic structure of the crust and upper mantle beneath the Great Plains, Rio Grande Rift, and Colorado Plateau using receiver functions, *J. Geophys. Res.*, *110*, B05306, doi:10.1029/2004JB003492.

Yang, Y., and D. Forsyth (2006), Regional tomographic inversion of the amplitude and phase of Rayleigh waves with 2-D sensitivity kernels, *Geophys. J. Int.*, *166*, 1148–1160.

Yang, Y., M. H. Ritzwoller, F.-C. Lin, M. P. Moschetti, and N. M. Shapiro (2008), Structure of the crust and uppermost mantle beneath the Western United States revealed by ambient noise and earthquake tomography, *J. Geophys. Res.*, *113*, B12, 1–9, doi:10.1029/2008JB005833.

Zandt, G., H. Gilbert, T. J. Owens, M. Ducea, J. Saleeby, and C. H. Jones (2004), Active foundering of a continental arc root beneath the southern Sierra Nevada in California, *Nature*, *431*, 41–46.